In the format provided by the authors and unedited.

Large anomalous Nernst effect at room temperature in a chiral antiferromagnet

Muhammad Ikhlas[1]*, Takahiro Tomita[1]*, Takashi Koretsune[2,3], Michi-To Suzuki[2], Daisuke Nishio-Hamane[1], Ryotaro Arita[2,4], Yoshichika Otani[1,2,4], Satoru Nakatsuji[1,4]

[1]*Institute for Solid State Physics, University of Tokyo, Kashiwa 277-8581, Japan*

[2]*RIKEN-CEMS, 2-1 Hirosawa, Wako 351-0198, Japan*

[3]*PRESTO, Japan Science and Technology Agency (JST), 4-1-8 Honcho Kawaguchi, Saitama 332-0012, Japan.*

[4]*CREST, Japan Science and Technology Agency (JST), 4-1-8 Honcho Kawaguchi, Saitama 332-0012, Japan.*

1 Expression of the Hall conductivity σ_{ji} and transverse thermoelectric conductivity α_{ji}

To compare the experimental results with first-principle calculation, we used the following expression for the Hall conductivity σ_{ji} and transverse thermoelectric conductivity α_{ji}, which take into account the anisotropy of the longitudinal resistivity ρ_{ii},

$$\sigma_{ji} \approx -\frac{\rho_{ji}}{\rho_{ii}\rho_{jj}}, \tag{1}$$

$$\alpha_{ji} \approx \frac{1}{\rho_{jj}}\left(S_{ji} - \frac{\rho_{ji}}{\rho_{ii}}S_{ii}\right) \tag{2}$$

---

*These two authors contributed equally.

Here, $(i, j) = (x, y)$, (y, z), and (z, x), where x, y, and z are taken to be the coordinates along $[2\bar{1}\bar{1}0]$, $[01\bar{1}0]$, and $[0001]$, respectively [1]. In our transport measurements, the applied current I (heat current $Q = -\nabla T$) is defined to be parallel to the i-axis. The longitudinal resistivity ρ_{ii} (Seebeck coefficient S_{ii}) is then measured using contacts placed along the i-axis while the Hall resistivity ρ_{ji} (Nernst signal S_{ji}) is measured using contacts located along the j-axis. Using this definition, the sign of the Hall and the Nernst effect is determined by the right-hand rule.

2   Temperature dependence of the longitudinal resistivity

The temperature dependence of the longitudinal resistivity for Sample 1 ($Mn_{3.06}Sn_{0.94}$) and Sample 2 ($Mn_{3.09}Sn_{0.91}$) single crystals used is given in Figure S1. Both Samples 1&2 show similar behaviour, i.e the in-plane resistivity is almost isotropic, while the out-of-plane resistivity shows a much stronger temperature dependence than the in-plane resistivity. The residual resistivity ratio (RRR = ρ (390 K) / ρ (4.2 K)) which is a rough measure of the quality of the single crystals shows the value of RRR $\sim 1.5 - 2.3$ for Sample 1 and RRR $\sim 1.2 - 1.35$ for Sample 2 in the in-plane direction, and ~ 3.5 for Sample 1 and ~ 2.8 for Sample 2 in the out-of-plane direction. This is consistent with the smaller coercivity observed in the Sample 1 crystals compared to Sample 2, as the coercivity in magnets generally increases with the number of defects and impurities, which may pin a magnetic domain wall. All the components of the longitudinal resistivity have continuous temperature change and nearly saturate above room temperature.

3 Magnetic field dependence of the Seebeck coefficient and the Nernst effect

The magnetic field dependence of the Seebeck coefficient S_{ii} $(i = x, y)$ was measured at various temperatures under B < 0.1 T along in-plane directions. We found no field dependence within experimental accuracy over all the temperature range between 50 K and 390 K. Figures S2a and S2b represent typical S_{xx} vs. B results obtained at 100 K and 300 K for Samples 1&2, respectively. The magnetic field dependences of the Nernst effect S_{zx} under B < 0.1 T along in-plane directions for Samples 1&2 are shown in Figures S2c and S2d, respectively.

4 Temperature dependence of the Seebeck effect

As shown in Figure 3c inset in the main text, $S_{ii}(T)$ $(i = x, y)$ of Sample 1 ($Mn_{3.06}Sn_{0.94}$) changes its sign below around 100 K and peaks with a negative amplitude at ~ 50 K. On the other hand, Figure 3d inset shows that a much weaker or nearly no sign change occurs for Sample 2 ($Mn_{3.09}Sn_{0.91}$). The Seebeck coefficient S generally has two contributions: $S = S_d + S_g$. S_d is the contribution from the charge carrier diffusion and S_g is the contribution from the phonon drag effect due to additional charge carriers dragged by the phonon flow. The effect of the phonon drag typically causes a peak in the Seebeck coefficient at $\sim \Theta_{\mathrm{D}}/5$, where Θ_{D} is the Debye temperature[2]. We made a linear fit to the temperature dependence of the specific heat divided by temperature (Supplementary Figure S3) at the lowest temperature region (2 −4.5 K) using the Einstein-Debye equation, $C/T = \gamma + \beta T^2$, where γ and β are the parameters for the electronic and lattice contributions to the specific heat, respectively. The fit gives $\beta = 0.300 \pm 0.015$ mJ mol^{-1} K^{-4} corresponding to the Debye temperature of $\Theta_{\mathrm{D}} = 280 \pm 14$ K. As shown in Figure 3c inset of the main text, the

minimum of the Seebeck coefficient is roughly located around $\Theta_D/5 = 56$ K, suggesting that the low temperature behaviour may be related to the phonon drag effect. The nearly no sign change in Sample 2 may be related to a larger amount of defects caused by doping, which reduces the phonon lifetime. However, further discussion on the temperature dependence of the Seebeck effect is beyond the scope of this paper, since the multiband nature of this system[3] would necessitate more involved analysis. On the other hand, the observed Nernst effect is dominated by the anomalous (spontaneous) contribution and thus transverse thermoelectric conductivity α_{ji} mainly comes from the Berry curvature. Therefore, the contribution from phonon drag in α_{ji} is negligible.

5   Crystal structure of Mn₃Sn

RAPID (Rigaku) X-ray diffractometer (MoKα, $\lambda = 0.7103$ Å) was used at room temperature to investigate the crystal structure of $\mathrm{Mn_3Sn}$. Two-dimensional Debye-Scherrer rings were obtained by the X-ray intensity transmitted through the sample, which were then converted to one-dimensional intensity patterns. The diffraction patterns were analyzed using the Rietveld analysis program RIETAN-FP to determine the precise crystal structure [4] . We assign a hexagonal structure ($P6_3/mmc$) with the lattice parameters $a =$5.662 Å and $c =$4.529 Å[5]. Figure S5 shows the typical result of the X-ray powder pattern obtained for Sample 1 ($\mathrm{Mn_{3.06}Sn_{0.94}}$). The atomic coordinates for the crystal parameter are shown in Table S1 for Sample 1 ($\mathrm{Mn_{3.06}Sn_{0.94}}$) and Table S2 for Sample 2 ($\mathrm{Mn_{3.09}Sn_{0.91}}$). Our results indicate that the samples used in our study have the same crystal structure as those used for previous neutron diffraction measurements[5,6] .

6 High-resolution transmission electron microscope (TEM) image of Mn$_3$Sn

Figures S6a and S6b show the high resolution TEM image of Mn$_3$Sn (using Sample 1 as a representative) taken at room temperature for the (0001) and $(2\bar{1}\bar{1}0)$ planes, respectively. Within the resolution permitted by the maximum operating voltage (200 kV) of the transmission electron microscope (JEOL JEM-2010F), the lattice parameters a and c obtained from the image are in good agreement with the results of our Rietveld analyses discussed above. The overlayed simulation images show the expected position of the Mn and Sn atoms within the lattice.

7 Heat treatment effect on the temperature dependence of the magnetization

A recent paper reported the magnetization curves for Mn$_3$Sn at different temperatures and found that the in-plane coercive field disappears along with the spontaneous magnetization as the sample is cooled down below 270 K[7]. In contrast to the temperature dependence of the magnetization of our crystal, an additional transition is observed below 270 K in both their magnetization and heat capacity data. They associated this with a transition from the triangular spin structure to a long-period helical spin configuration, which has been observed in earlier neutron scattering studies[8]. It has been known that this transition is observed most pronouncedly in single crystals that were annealed at temperatures below 800°C[9]. Their single crystals were synthesized by slow-cooling the melt from 1000°C to 600°C, and thus a part of this slow-cooling process may play a role of the annealing procedure mentioned above. The mechanism behind this transition is still unknown. On the other hand, the single crystal used in our present paper was prepared from the Bridgman furnace without any additional annealing process, and thus exhibit no transition above 50 K[10].

8 Relation between the anomalous Nernst effect and the anomalous Hall conductivity

Both the intrinsic anomalous Hall conductivity σ_{zx} and the intrinsic anomalous transverse thermo-electric conductivity α_{zx} are governed by the Berry curvature, $\mathbf{\Omega}_n(\mathbf{k})$, as[11]

$$\sigma_{zx} = -\frac{e^2}{\hbar} \int \frac{d\mathbf{k}}{(2\pi)^3} \Omega_{n,y}(\mathbf{k}) f_{n\mathbf{k}}, \tag{3}$$

$$\alpha_{zx} = -\frac{e}{T\hbar} \int \frac{d\mathbf{k}}{(2\pi)^3} \Omega_{n,y}(\mathbf{k}) \left\{ (\varepsilon_{n\mathbf{k}} - \mu) f_{n\mathbf{k}} + k_{\mathrm{B}}T \ln \left[1 + e^{-\beta(\varepsilon_{n\mathbf{k}} - \mu)} \right] \right\}. \tag{4}$$

Here, $\varepsilon_{n\mathbf{k}}, f_{n\mathbf{k}}$ are the band energy and the Fermi-Dirac distribution function with the band index n and the wave vector $\mathbf{k}$. Since $\left\{ (\varepsilon_{n\mathbf{k}} - \mu) f_{n\mathbf{k}} + k_{\mathrm{B}}T \ln \left[1 + e^{-\beta(\varepsilon_{n\mathbf{k}} - \mu)} \right] \right\}$ is finite only around the Fermi energy, α_{zx} is determined by the Berry curvature around the Fermi energy whereas σ_{zx} is the summation of all the Berry curvature below the Fermi energy. According to these equations, α_{zx} and σ_{zx} are related as follows:

$$\alpha_{zx} = -\frac{1}{e} \int d\varepsilon \frac{\partial f}{\partial \mu} \sigma_{zx}(\varepsilon) \frac{\varepsilon - \mu}{T}. \tag{5}$$

Thus, the size and the sign of α_{zx} are determined by the slope of $\sigma_{zx}(\varepsilon)$ as well as the Berry curvature around the Fermi energy. Indeed, at low temperatures, Eq.(5) can be approximated as

$$\alpha_{zx} = \frac{\pi^2 k_B^2 T}{3|e|} \frac{\partial \sigma_{zx}(\varepsilon)}{\partial \varepsilon} + O(T^3). \tag{6}$$

Supplementary Figure S4 indicates the calculated result of the energy dependence of the anomalous Hall and transverse thermoelectric conductivity. According to the result, a slight shift of the Fermi energy leads to a change in the anomalous Hall conductivity. For example, at $\varepsilon = 0.04$ eV, $-\partial\sigma_{zx}/\partial\varepsilon \sim 1000 \ (\Omega\mathrm{cm})^{-1}(\mathrm{eV})^{-1}$. This means that $-\alpha_{zx} \sim 0.0024T$ (A/Km) at low temperature limit, which is consistent with the value of $-\alpha_{zx} = 0.25$ (A/Km) at $T = 100$ K in the inset of Fig. 3f.

In our first-principles calculation for Mn_3Sn, the number of the Mn-s, Mn-d, Sn-s, Sn-p electrons are estimated to be 0.84, 5.85, 1.67, and 3.26, respectively. For $Mn_{3.06}Sn_{0.94}$, we can assume that the electron occupancy of the Sn-s, Sn-p and Mn-s orbital are the same as those of Mn_3Sn, since the low-energy states around the Fermi level are mainly formed by the Mn-d orbital. Then the number of electrons doped into the Mn-d orbital is estimated to be 0.024, which shifts the Fermi energy by 0.04 eV for $Mn_{3.06}Sn_{0.94}$. With a similar calculation, the shift of the Fermi energy is estimated to be 0.05 eV for $Mn_{3.09}Sn_{0.91}$.

In experiment, a small change in the composition in the crystals used in the present study, namely $Mn_{3.06}Sn_{0.94}$ and $Mn_{3.09}Sn_{0.91}$, may cause such a shift in E_F. Although the Hall conductivity between the two crystals are almost the same at high temperatures, the difference between the Hall conductivity of the two crystals becomes apparent at low temperatures, as shown in Fig. 3e in the main text. At 100 K, Sample 2 ($Mn_{3.09}Sn_{0.91}$) shows larger anomalous Hall conductivity (lower anomalous transverse thermoelectric conductivity) than Sample 1 ($Mn_{3.06}Sn_{0.94}$), which semi-quantitatively agrees with first principle-calculation shown in Figure S4. Further investigation is necessary to make a more thorough, quantitative comparison between experiment and theory using samples with a variety of doping levels, and this defines a subject of future study.

The DFT calculation does not take account of the temperature dependence of the local magnetic moment size. Generally, the states further apart from the Fermi energy are more affected by the change in the moment size. Thus, in comparison with the transverse thermoelectric conductivity, the theoretical estimate for the Hall conductivity is expected to have the larger deviation from experiment. This is because according to Eqs. (3) & (4), the Hall effect is the sum of Berry curva-

ture of all occupied bands, while the transverse thermoelectric conductivity only derives from the low energy states around E_F. In fact, we found that the disagreement between the theoretical and experimental values of the Hall conductivity is larger than the one for the transverse thermoelectric conductivity (Fig. 3 in the main text).

Supplementary Figure S1. Temperature dependences of the longitudinal resistivity in Mn$_3$Sn

Temperature dependence of the longitudinal resistivity $\rho_{ii}(T)$ ($i = x$ (red), y (blue), and z (green)) of **a**, Sample 1 (Mn$_{3.06}$Sn$_{0.94}$) and **b**, Sample 2 (Mn$_{3.09}$Sn$_{0.91}$) measured at zero field.

Supplementary Figure S2. Magnetic field dependences of the Seebeck coefficient and Nernst effect in Mn$_3$Sn

a, Field dependence of the Seebeck coefficient S_{ii} ($i = x, y$) at 100 K and 300 K for Sample 1 (Mn$_{3.06}$Sn$_{0.94}$). **b**, Field dependence of the Seebeck coefficient S_{ii} ($i = x, y$) at 100 K and 300 K for Sample 2 (Mn$_{3.09}$Sn$_{0.91}$). **c**, Field dependence of the Nernst effect $-S_{zx}$ of Sample 1 (Mn$_{3.06}$Sn$_{0.94}$) at 350 K, 300 K, 200 K, and 50 K. **d**, Field dependence of the Nernst effect $-S_{zx}$ of Sample 2 (Mn$_{3.09}$Sn$_{0.91}$) at 300 K and 200 K. The error-bars are shown if they are larger than the symbol sizes and indicate the measurement errors that come from the uncertainties of their geometrical factors (Methods)

Supplementary Figure S3. Temperature dependence of the specific heat in Mn$_3$Sn

Specific heat of Sample 1 (Mn$_{3.06}$Sn$_{0.94}$) single crystal divided by temperature C/T (red circle) measured in zero magnetic field, plotted vs. T^2. The blue solid line indicates a linear fit at the low temperature region, $2 \leq T \leq 4.5$ K, to estimate γ and β in the Einstein-Debye equation $C/T = \gamma + \beta T^2$. The fit gives the values $\gamma = $ 22.7 ± 0.2 mJ mol^{-1} K^{-2} and

$\beta = 0.300 \pm 0.015$ mJ mol^{-1} K^{-4}.

Supplementary Figure S4. Energy dependence of the anomalous Hall conductivity and anomalous transverse thermoelectric conductivity

Energy dependence of **a,** the anomalous Hall conductivity $-\sigma_{zx}$, and **b,** the anomalous transverse thermoelectric conductivity $-\alpha_{zx}$ at $T = 100$ K obtained by the first-principles calculation. E_{F} stands for the Fermi energy for the stoichiometric Mn$_3$Sn.

Supplementary Figure S5. X-ray diffraction pattern for Mn$_3$Sn

Room temperature X-ray diffraction (XRD) patterns of Sample 1 Mn$_{3.06}$Sn$_{0.94}$. The crosses correspond to experimental data and the solid line (red) is for the Rietveld refinement fit. Vertical bars (green) below the curves indicate the peak positions of Mn$_3$Sn phase. The lower curve (blue) is the difference between the observed and calculated at each step.

Supplementary Figure S6. Transmission electron microscope image

Bright field high resolution lattice image projected from **a**, [0001] and **b**, [$2\bar{1}\bar{1}0$] directions, compared with simulation image.

1. Kiyohara, N., Tomita, T. & Nakatsuji, S. Giant Anomalous Hall Effect in the Chiral Antiferromagnet Mn$_3$Ge. *Phys. Rev. Applied* **5**, 064009 (2016).

2. Ziman, J. M. *Electrons and phonons: the theory of transport phenomena in solids* (Oxford University Press, 1960).

3. Yang, H. *et al.* Topological Weyl semimetals in the chiral antiferromagnetic materials Mn$_3$Ge and Mn$_3$Sn. *New J. Phys.* **19**, 015008 (2017).
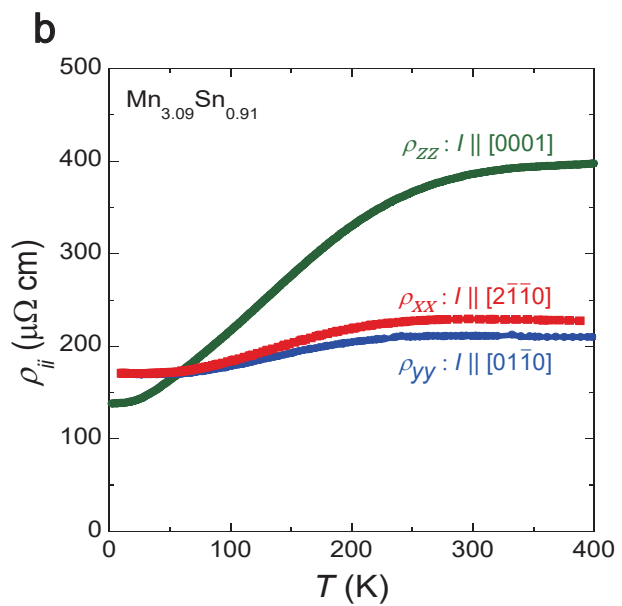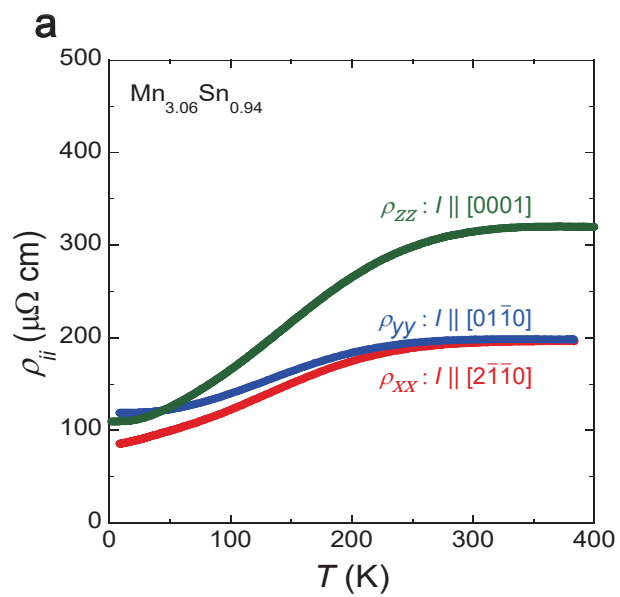
4. Izumi, F. & Momma, K. Three-dimensional visualization in powder diffraction. In *Solid State Phenomena*, vol. 130, 15–20 (Trans Tech Publ, 2007).

5. Tomiyoshi, S. Polarized neutron diffraction study of the spin structure of Mn_3Sn. *J. Phys. Soc. Jpn.* **51**, 803–810 (1982).

6. Brown, P. J., Nunez, V., Tasset, F., Forsyth, J. B. & Radhakrishna, P. Determination of the magnetic structure of Mn_3Sn using generalized neutron polarization analysis. *J. Phys. Condens. Matter.* **2**, 9409–9422 (1990).

7. Duan, T. *et al.* Magnetic anisotropy of single-crystalline Mn_3Sn in triangular and helix-phase states. *App. Phys Lett* **107**, 082403 (2015).

8. Cable, J. W., Wakabayashi, N. & Radhakrishna, P. Magnetic excitations in the triangular antiferromagnets Mn_3Sn and Mn_3Ge. *Phys. Rev. B* **48**, 6159–6166 (1993).

9. Ohmori, H., Tomiyoshi, S., Yamauchi, H. & Yamamoto, H. Spin structure and weak ferromagnetism of Mn_3Sn. *J. Magn. Magn. Mater.* **70**, 249–251 (1987).

10. Tomiyoshi, S., Abe, S., Yamaguchi, Y., Yamauchi, H. & Yamamoto, H. Triangular spin structure and weak ferromagnetism of Mn_3Sn at low temperature. *J. Magn. Magn. Mater.* **54**, 1001–1002 (1986).

11. Xiao, D., Yao, Y., Fang, Z. & Niu, Q. Berry-phase Effect in Anomalous Thermoelectric Transport. *Phys. Rev. Lett.* **97**, 026603 (2006).

Table S1: Crystal structure parameters refined by Rietveld analysis for $Mn_{3+0.06}Sn_{1-0.06}$ (Sample 1) with $P6_3/mmc$ structure at 300 K. The lattice parameters and the atomic positions of the Mn site are determined by the analysis, which is made using the X-ray diffraction spectra with MoKα radiation ($\lambda = 0.7103$ Å). The final R indicators are R_{WP}=5.29, R_e=9.45, and S=0.560 [4].
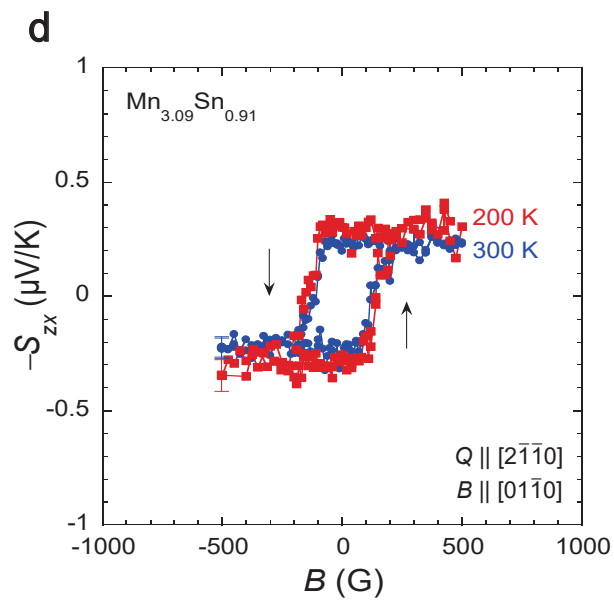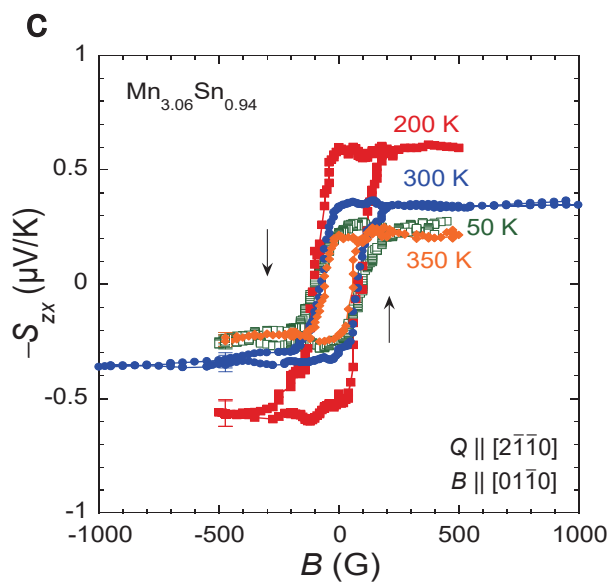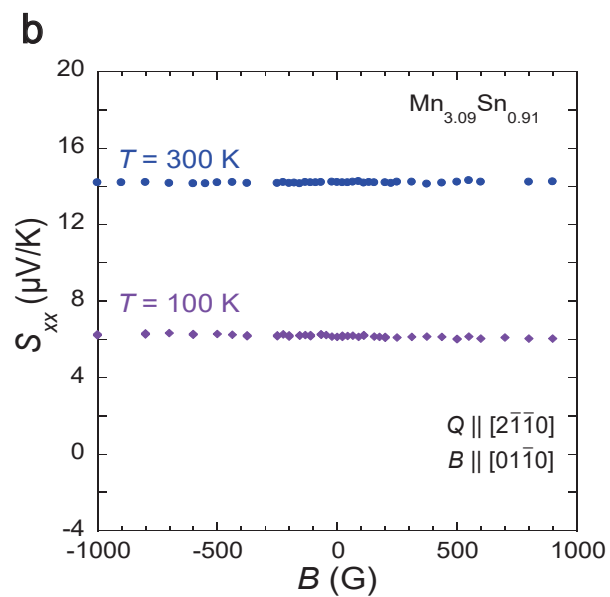
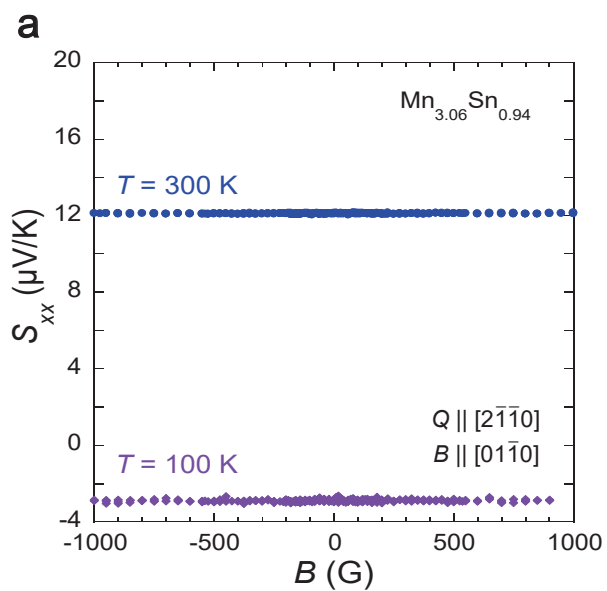| $Mn_{3+0.06}Sn_{1-0.06}$		$V = 125.747(8)$ Å^3			
parameters (Å)		$a = 5.6624(2)$	$b = 5.6624(2)$	$c = 4.5286(2)$	
Atom	Wyckoff position	x	y	z	Occupancy
Mn	6h	0.8388(2)	0.6777(3)	1/4	1
Sn/Mn	2c	1/3	2/3	1/4	(0.94/0.06)

Table S2: Crystal structure parameters refined by Rietveld analysis for $Mn_{3+0.09}Sn_{1-0.09}$ (Sample 2) with $P6_3/mmc$ structure at 300 K. The lattice parameters and the atomic positions of the Mn site are determined by the analysis, which is made using the X-ray diffraction spectra with MoKα radiation ($\lambda = 0.7103$ Å). The final R indicators are R_{WP}= 4.35, R_e=13.0, and S=0.334 [4].

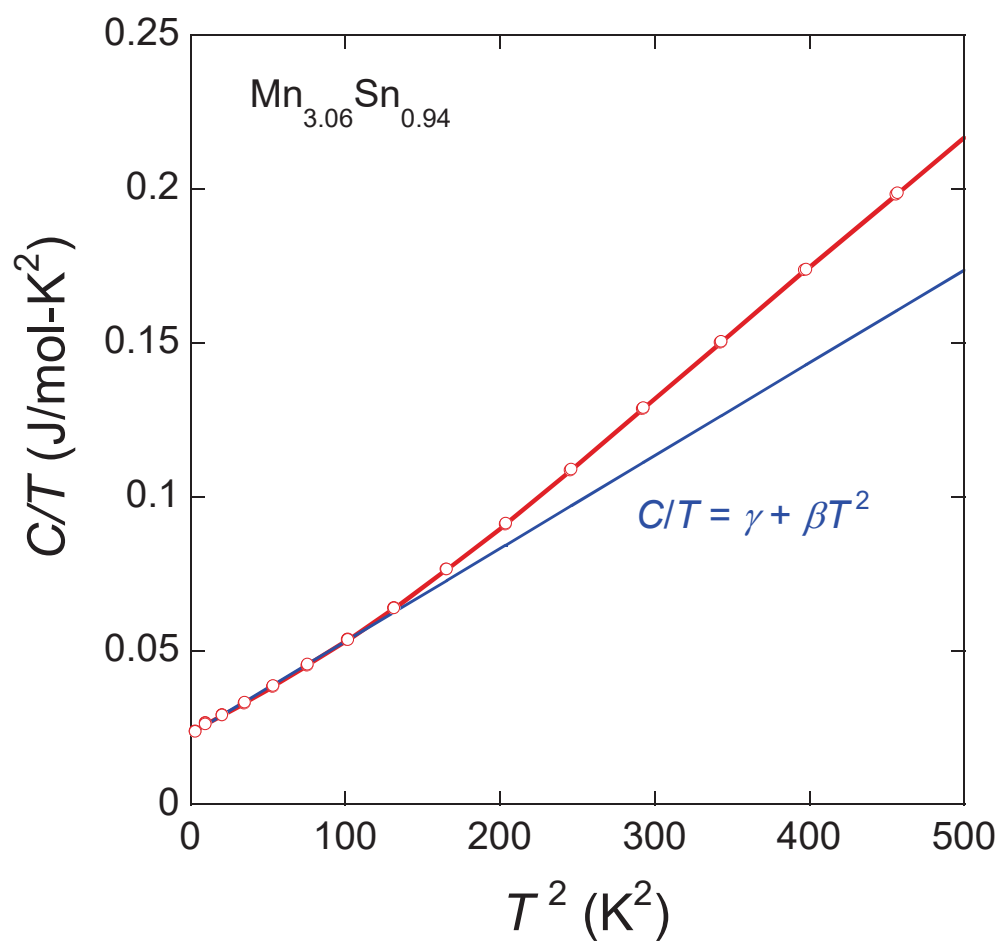| $Mn_{3+0.09}Sn_{1-0.09}$		125.623(9) Å^3			
parameters (Å)		$a = 5.6587(2)$	$b = 5.6587(2)$	$c = 4.5300(2)$	
Atom	Wyckoff position	x	y	z	Occupancy
Mn	6h	0.8402(2)	0.6803(3)	1/4	1
Sn/Mn	2c	1/3	2/3	1/4	(0.91/0.09)

a Mn$_{3.06}$Sn$_{0.94}$

ρ_{zz}: $I \parallel$ [0001]

ρ_{yy}: $I \parallel$ [01$\bar{1}$0]

ρ_{xx}: $I \parallel$ [2$\bar{1}\bar{1}$0]

ρ_{ii} ($\mu\Omega$ cm)

T (K)

b Mn$_{3.09}$Sn$_{0.91}$

ρ_{zz}: $I \parallel$ [0001]

ρ_{xx}: $I \parallel$ [2$\bar{1}\bar{1}$0]
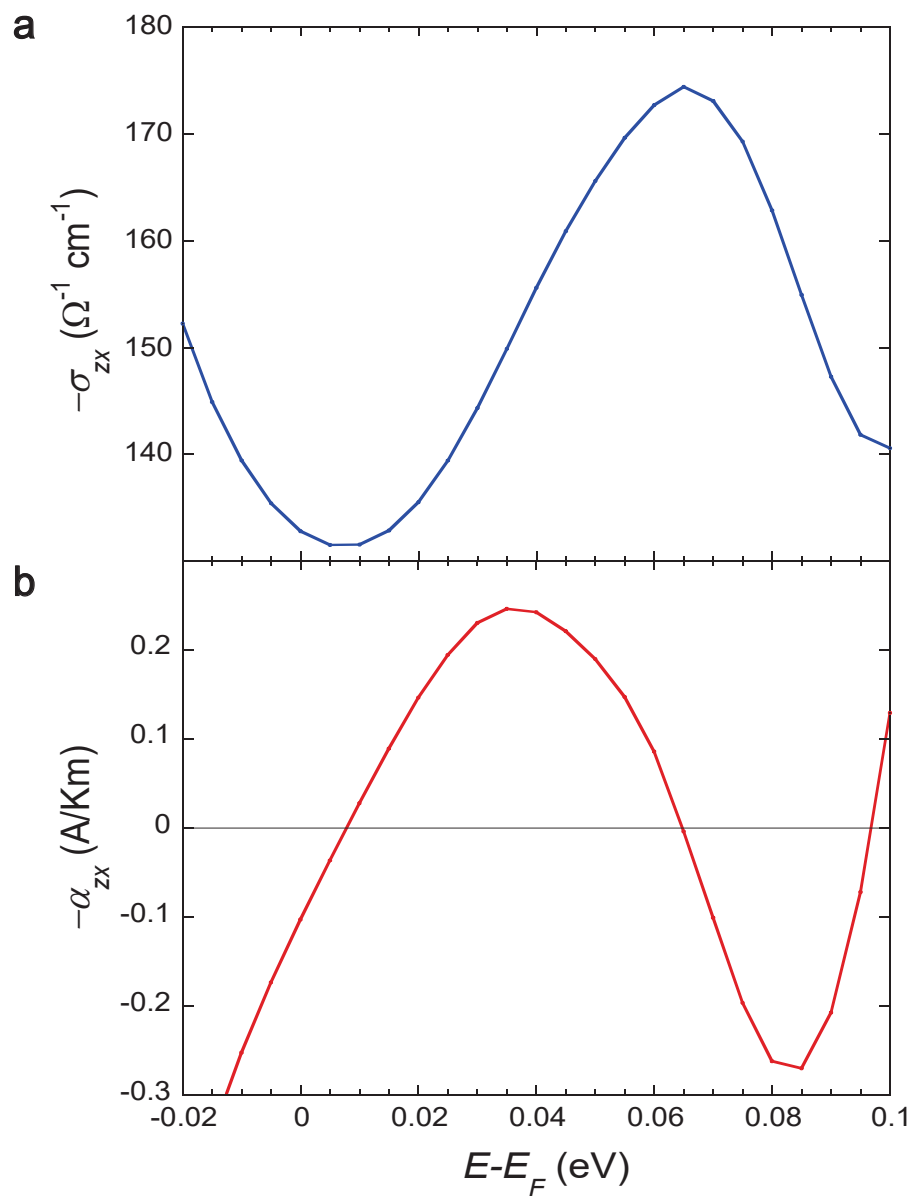
ρ_{yy}: $I \parallel$ [01$\bar{1}$0]

ρ_{ii} ($\mu\Omega$ cm)

T (K)

Supplementary Figure S1
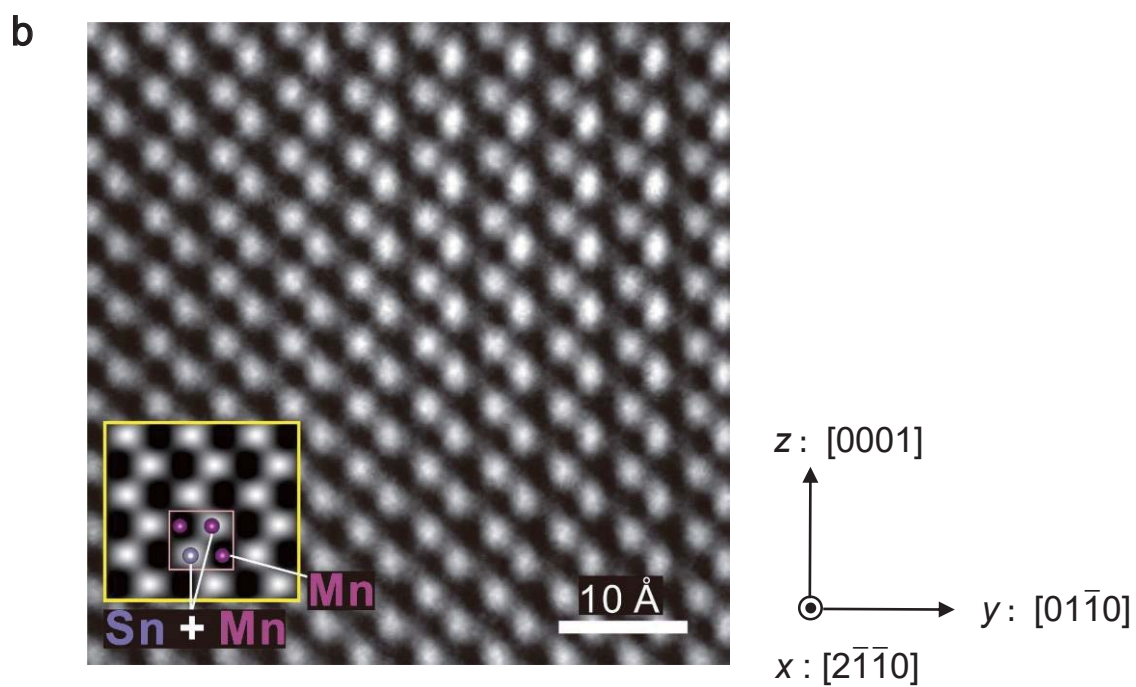
Supplementary Figure S2

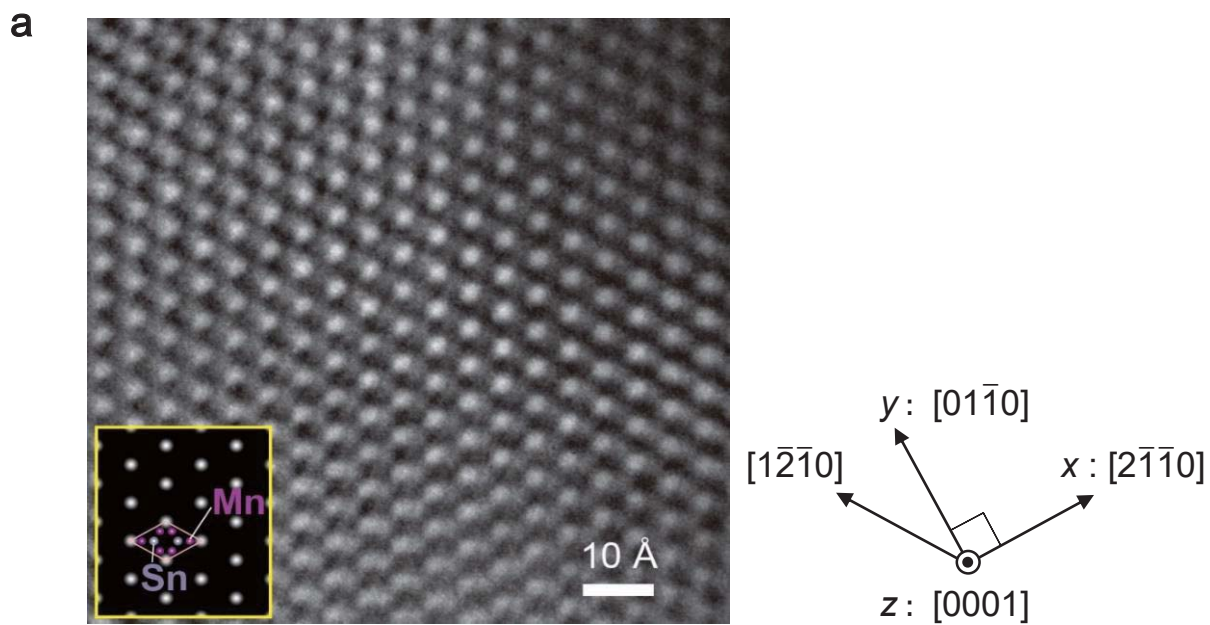$Mn_{3.06}Sn_{0.94}$

$C/T = \gamma + \beta T^2$

Supplementary Figure S3

Supplementary Figure S4

Supplementary Figure S5

a

y : [01$\bar{1}$0]

[1$\bar{2}$$\bar{1}$0]

x : [2$\bar{1}$$\bar{1}$0]

z : [0001]

b

z : [0001]

y : [01$\bar{1}$0]

x : [2$\bar{1}$$\bar{1}$0]

Supplementary Figure S6